Supporting Information

High-performance $Ti_xFe_{1-x}NbO_4$ fast-charging anodes sputtered and aggregated on paraffin oil interface

Shiying Luo,[a] Huanxin Huo,[a,b] Guodong Liu,[a] Zaohui Ding,[c] Libo Deng,*[b] Manlin Tan[d] and Lei Yao *[a]

[a] Guangdong Provincial Key Laboratory of New Energy Materials Service Safety, College of Materials Science and Engineering, Shenzhen University, Shenzhen, 518060, China
[b] College of Chemistry and Environmental Engineering, Shenzhen University, Shenzhen, 518060, China
[c] Shenzhen Bona Pharma Technology Co., Ltd, Shenzhen, 518060, China
[d] Research Institute of Tsinghua University in Shenzhen, 518057, China
* Corresponding author: Libo Deng (denglb@szu.edu.cn), Lei Yao (lyao@szu.edu.cn)

Experimental Section

Materials

All chemicals were used as received without further purification. Iron oxide (Fe_2O_3, 99.9%), and Titanium niobium oxide (TNO, 99.9%) were purchased from Shijiazhuang Jinshi Metal Materials Technology Co., Ltd. Alumina crucibles (Ø100 mm, Ø120 mm) were supplied by Ximu Instrument Equipment Co., Ltd. Paraffin oil (99.9%) was obtained from Sino Biological Engineering (Shanghai) Co., Ltd., while paraffin wax (analytical grade) was purchased from Hebei Wanshun Paraffin Products Co., Ltd. Quartz tubes (Ø150 mm) were purchased from Aopusi Quartz Products Co., Ltd. The commercial electrolyte ($LiPF_6$ in EC/DMC) for $LiFePO_4$ half-cell assembly was purchased from Suzhou Duoduo Experimental Instrument Co., Ltd. Aluminum foil (battery grade), copper foil (battery grade), coin cell cases (CR2032 type), Celgard 2400 separator, conductive carbon black (battery grade), and N-methyl-2-pyrrolidone (NMP, analytical grade) were obtained from Shenzhen Boyuan New Energy Technology Co., Ltd. Polyvinylidene fluoride (PVDF, analytical grade) was purchased from Solvay (China) Specialty Polymers Co., Ltd. High-purity argon (99.9%) and nitrogen (99.9%) gases were provided by Guangzhou Puyuan Industrial Gas Co., Ltd.

Preparation of self-supporting Ti-FNO films.

Al_2O_3 ceramic plates (diameter: 100 mm) were sequentially cleaned with ultrapure water and anhydrous ethanol. Subsequently, 1000 μl of paraffin oil was dropped onto the ceramic plate and evenly spread to serve as a liquid substrate for the fabrication of self-supporting oxide films. The liquid substrate was placed on a sample stage and transferred into the sputtering chamber by a robotic arm. The rotation speed of the sample stage was adjusted to 15 r min^{-1}. When the chamber pressure reached 9×10^{-4} Pa, Ar and O_2 gases were introduced. After 15 min of stabilization, the chamber pressure was adjusted to 5 Pa using a gas valve. Following the input of power and sputtering parameters, plasma ignition was initiated. After ignition, the chamber pressure was further tuned to 1 Pa to commence the formal sputtering process. Upon completion, the as-deposited film attached to the ceramic substrate was obtained.

To separate the film, the ceramic plate was placed in a Petri dish, into which petroleum ether was slowly added until the ceramic plate was completely immersed. After standing for sufficient time to fully dissolve the paraffin oil, the residual petroleum ether was removed. Anhydrous ethanol was

then added to replace the solvent, and the freestanding film was carefully collected using tweezers. The film was subsequently rinsed with ethanol and deionized water, followed by drying. Finally, the film was placed in an alumina crucible and calcined in a tubular furnace under a nitrogen atmosphere at a heating rate of 5 °C min^{-1} with a dwell time of 180 min.

Preparation of Ti-FNO by conventional solid-state reaction (C-SSR).

Weigh titanium niobate powder and iron oxide powder according to the stoichiometric ratio of Ti-doped iron niobate, and place them together into a zirconia milling jar. Add zirconia grinding balls at a ball-to-powder weight ratio of approximately 10:1, and mill at a rotation speed of 300 $r \cdot min^{-1}$ for 2 h. After milling, separate the resulting powder from the grinding balls by sieving, transfer it into an alumina crucible, and place the crucible in a muffle furnace. Under an air atmosphere, heat the powder to 1000 °C at a heating rate of 5 $°C \cdot min^{-1}$ to carry out the solid-state reaction, then allow the furnace to cool naturally to room temperature. Remove the product and grind it again into a fine powder to obtain the Ti-doped iron niobate powder.

Electrode preparation.

The calcined films were ground into fine powders using an agate mortar. A mixture of active material, conductive carbon black, and polyvinylidene fluoride (PVDF) binder in a mass ratio of 8:1:1 was prepared. N-methyl-2-pyrrolidone (NMP) was added as the solvent, and the slurry was homogenized in a vacuum mixer. The resulting slurry was uniformly coated onto Cu foil using a doctor blade with a controlled thickness. The coated electrodes were dried overnight in a vacuum oven at 80 °C, then punched into circular electrodes (12 mm in diameter) using a coin-cell punching machine. The mass of the active material on each electrode was recorded.

Electrochemical measurements.

CR2032-type half-cells were assembled to evaluate the electrochemical performance. The working electrode consisted of Ti-FNO coated on Cu foil, while lithium metal foil served as the counter/reference electrode. A Celgard polypropylene membrane (17 mm diameter) was used as the separator. The electrolyte was 1 M $LiPF_6$ dissolved in a mixture of ethylene carbonate (EC) and diethyl carbonate (DEC) (v/v = 1:1). Cell assembly was carried out in an Ar-filled glovebox (H_2O < 0.1 ppm, O_2 < 0.1 ppm) to ensure a moisture- and oxygen-free environment. The mass loading of the active material on the current collector was precisely controlled at 1.0–1.2 mg cm^{-2} for all tested electrodes. The thickness of the dried electrode film was measured as 60 μm using a high-precision

thickness gauge.

Characterization and Electrochemical Measurement

X-ray diffraction (XRD). XRD analysis was employed to investigate the phase composition, crystallinity, and lattice parameters of the materials. In this work, a Bruker D8 X-ray diffractometer (Bruker, Germany) was used with Cu Kα radiation (λ=0.15142 nm). The operating voltage and current of the X-ray tube were 40 kV and 200 mA, respectively. Data were collected over a 2θ range of 10–90° at scanning rates of 5° min^{-1} and 10° min^{-1}.

Field-emission scanning electron microscopy (FE-SEM). Surface morphology evolution of the films annealed at different temperatures (600–1000 °C) was observed using a SU8010 FE-SEM (Hitachi, Japan) with a magnification range of 1–10k and a working distance adjustable between 54–75 nm. FE-SEM analysis provided essential guidance for optimizing the film fabrication process.

Transmission electron microscopy (TEM). TEM characterization was performed on a JEM-F200 (JEOL, Japan) instrument with an accelerating voltage of 80–200 kV to examine the surface morphology and crystal structure of the films. Selected area electron diffraction (SAED) patterns allowed accurate identification of phase composition, while lattice fringes in high-resolution TEM (HRTEM) images were used to determine crystal orientation and interplanar spacing. Grain size distribution was statistically analyzed using ImageJ software.

X-ray photoelectron spectroscopy (XPS). XPS measurements were conducted using an ESCALAB 250Xi system (Thermo Fisher Scientific) with a monochromatic Al Kα X-ray source (1486.6 eV). High-resolution spectra were deconvoluted to identify the chemical states of the elements present.

Electrochemical measurements.

Galvanostatic charge–discharge (GCD) testing was performed on a 5V10Ma8CT system (LANHE) to evaluate the discharge/charge capacities and rate performance of Ti-FNO electrodes at various current densities.

Cyclic voltammetry (CV) and **electrochemical impedance spectroscopy (EIS)** were conducted on a CHI760E electrochemical workstation (Shanghai Chenhua Instruments) over a frequency range of 0.01–100 kHz.

For EIS testing, a small-amplitude sinusoidal voltage was applied to the cell over a frequency range from high frequency (100 kHz) to low frequency (0.01 Hz), and the resulting current response

was measured to calculate impedance. The impedance spectrum was typically presented as a Nyquist plot, showing a semicircle at high frequency and a straight line at low frequency. Equivalent circuit modeling, such as the Randles circuit, was used to extract key parameters, including solution resistance (R_s), charge-transfer resistance (R_{ct}), double-layer capacitance (C_{dl}), and Warburg impedance (Z_w). The Warburg impedance, associated with Li^+ diffusion in the electrode, manifests as a 45° slope in the low-frequency region and is inversely proportional to the square root of frequency.

The Warburg coefficient (σ) was obtained by fitting the low-frequency region:

$$Z^{'} = R_1 + R_{ct} + \sigma\omega^{-\frac{1}{2}}$$

where Z' is the real part of the impedance and $\omega = 2\pi f$ is the angular frequency. The Li^+ diffusion coefficient (D) was then calculated using the following relation:

$$D_{Li+} = R^2T^2/2S^2n^2F^4C^2\sigma^2$$

where F is the Faraday constant, A is the electrode area, n is the number of electrons transferred per reaction, R is the gas constant, C is the molar concentration of Li^+ in the electrolyte, and T is the absolute temperature.

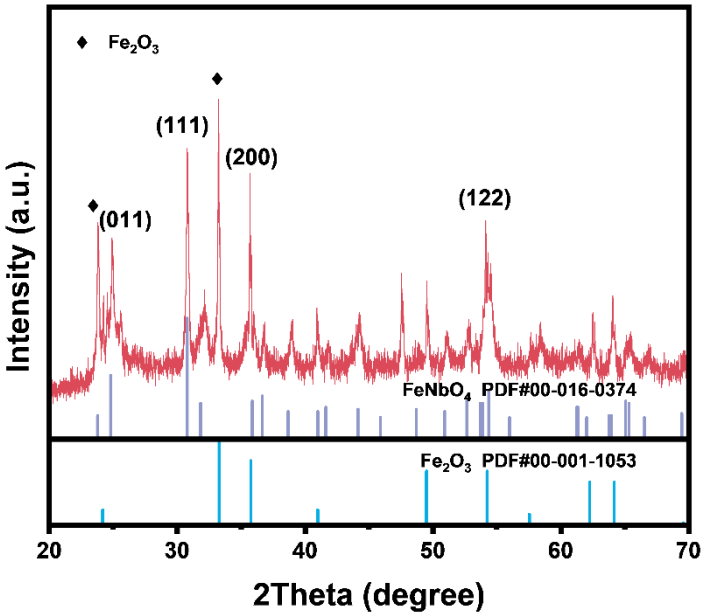

Fig. S1. $FeNbO_4$ prepared by the C-SSR at 1000 °C.

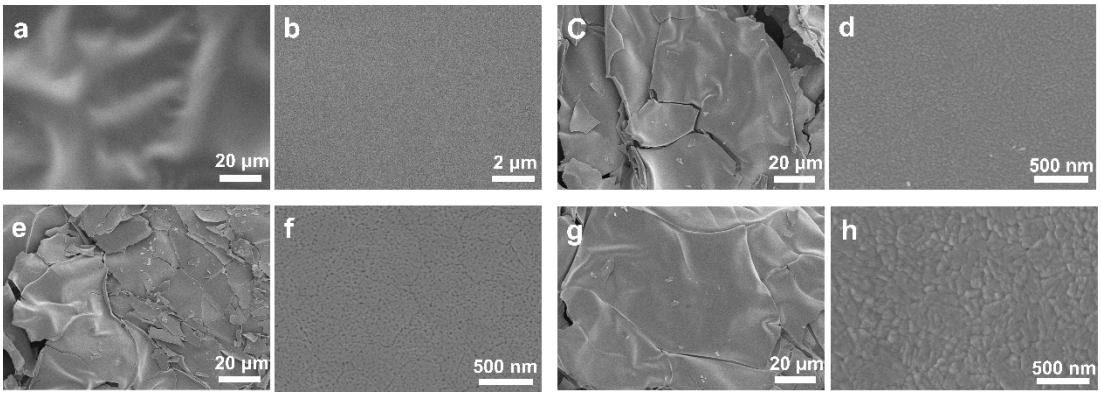

Fig. S2. SEM images of Ti-FNO films annealed at different temperatures: (a) and (b) as-deposited at 25 °C; (c) and (d) annealed at 600 °C; (e) and (f) at 700 °C; (g) and (h) at 900 °C.

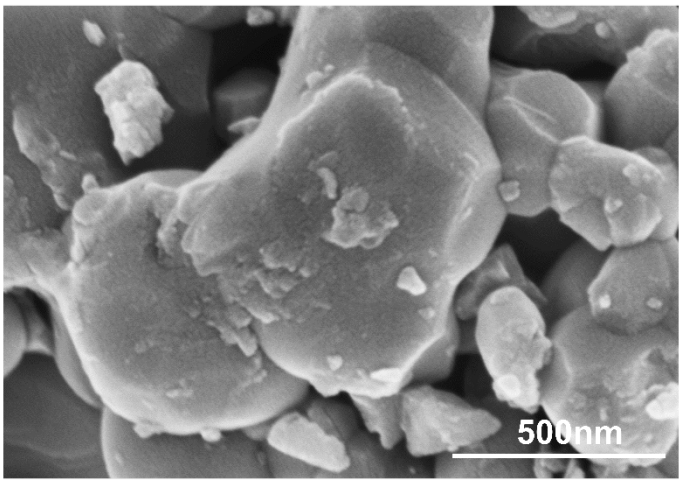

Fig. S3. SEM images of Ti-doped $FeNbO_4$ prepared by the C-SSR method calcined at 1000 °C.

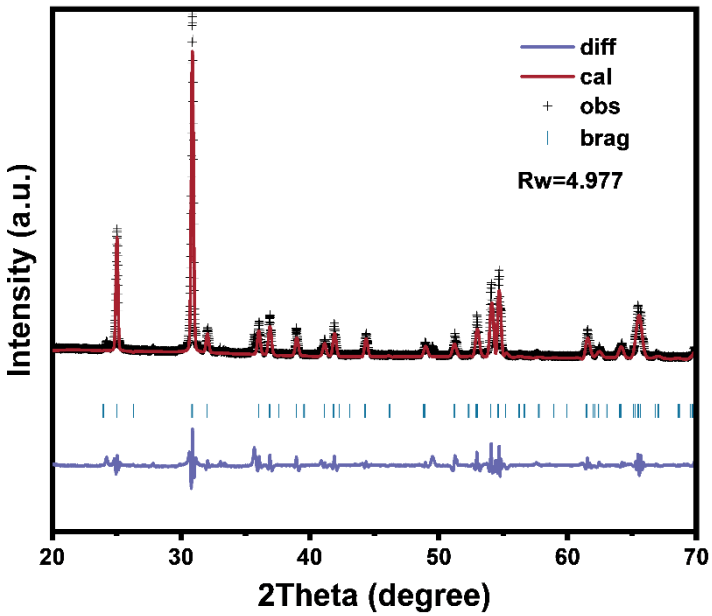

Fig. S4. Rietveld Refined XRD spectra of Ti-FNO.

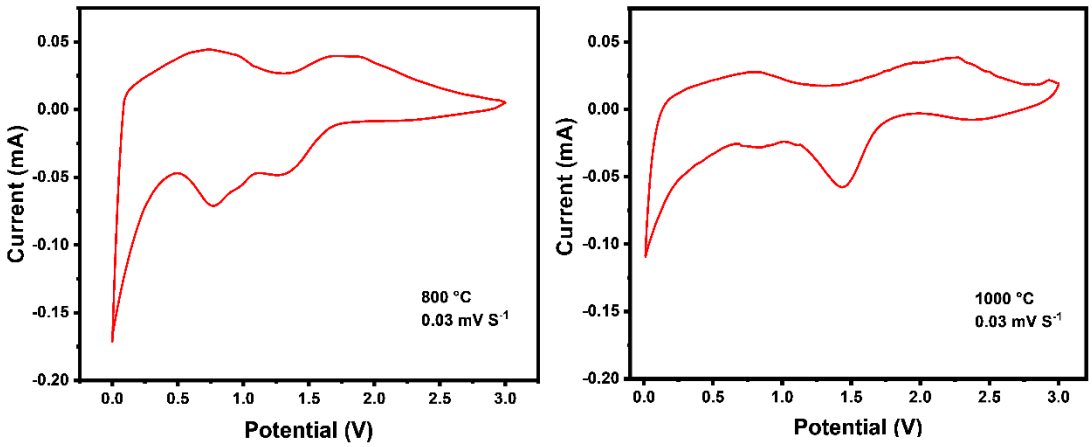

Fig. S5. Electrochemical performance of Ti-FNO of CV curves at a scan rate of 0.03 mV s^{-1}.

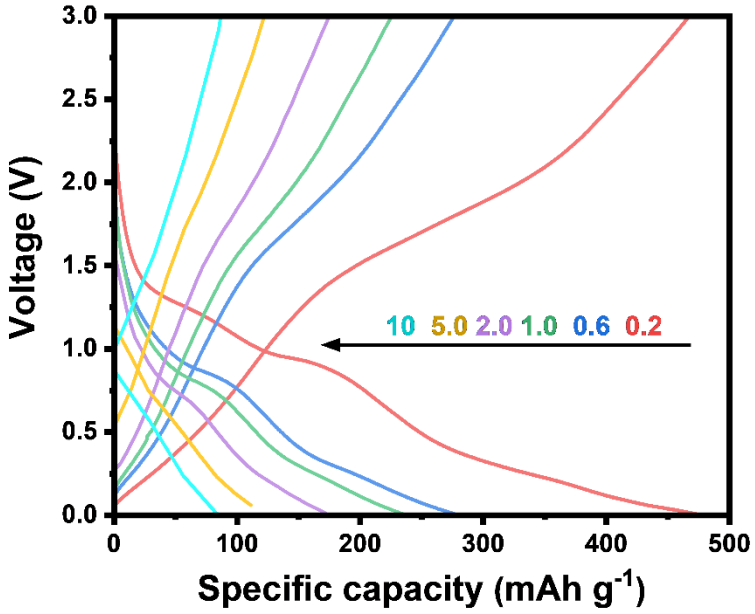

Fig. S6. Charge-discharge curves of the pure-phase Ti-FNO battery at various current densities.

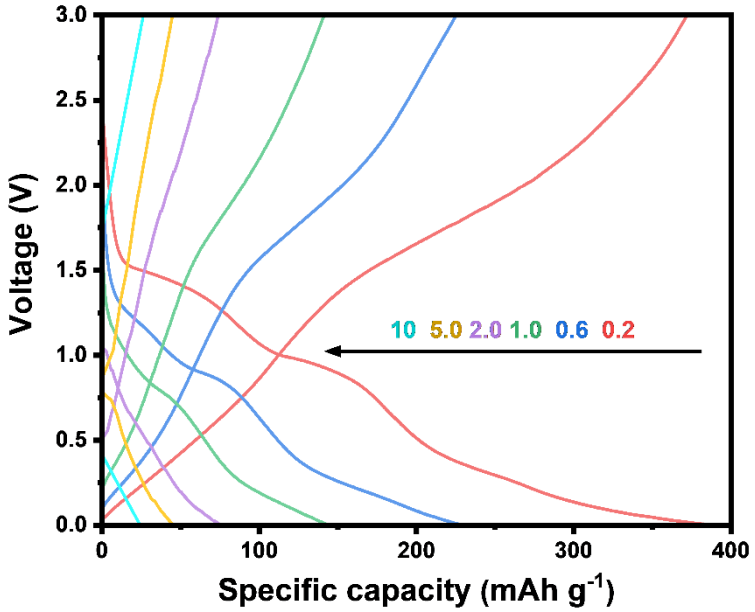

Fig. S7. Charge-discharge curves of the mixed-phase Ti-FNO battery at various current densities.

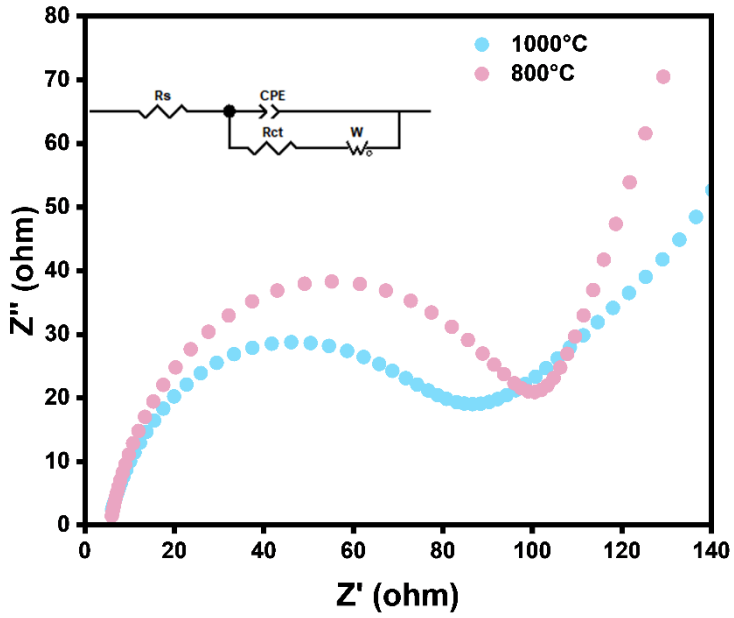

Fig. S8. EIS plots of pure-phase Ti-FNO and mixed-phase Ti-FNO batteries.

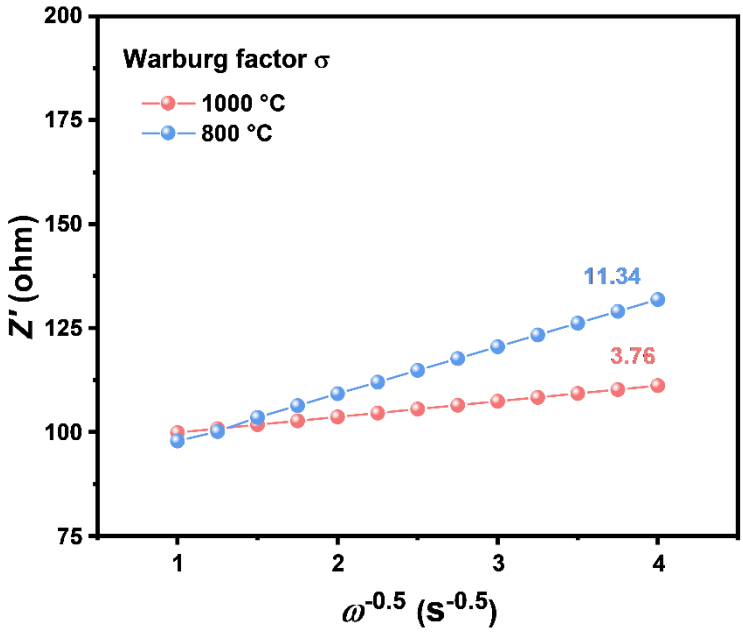

Fig. S9. Fitting curves of resistance (Z') versus the square root of angular frequency ($\omega^{-0.5}$).

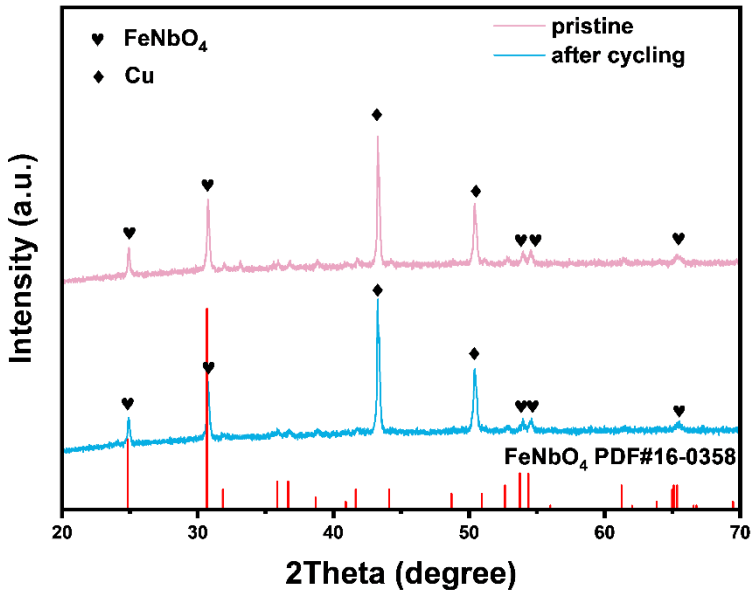

Fig. S10. XRD patterns of T-FNO electrode before and after cycling.

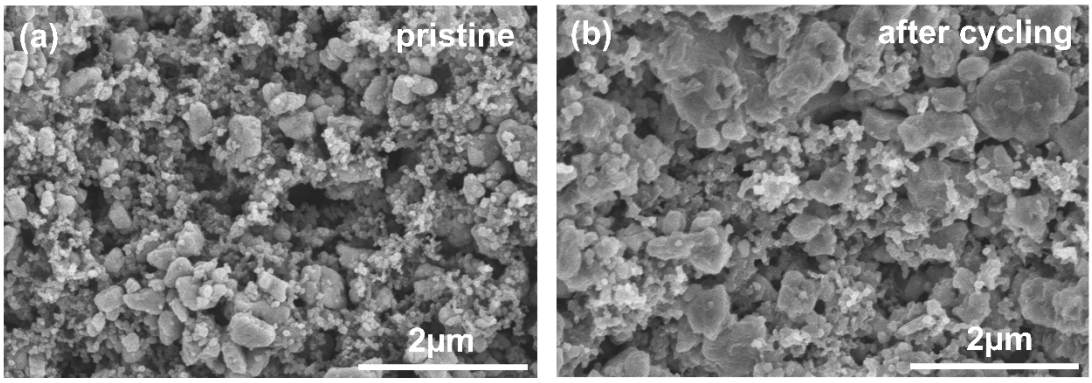

Fig. S11. SEM images of T-FNO electrode (a) before and (b) after cycling for 8000 cycles.

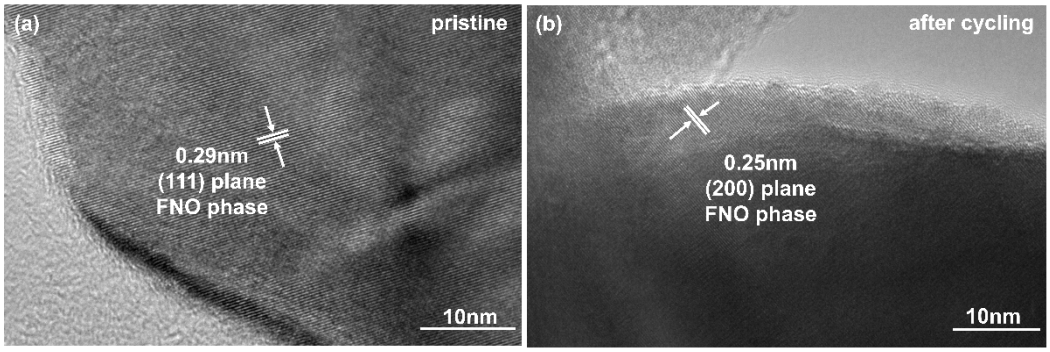

Fig. S12. HRTEM images of T-FNO electrode (a) before and (b) after cycling for 8000 cycles.

Table S1. The unit cell parameters obtained by XRD refinement of Ti-FNO samples were compared with the standard unit cell parameters.

Sample	Cell parameter (Å)			V (Å^3)
	a	*b*	*c*	
Ti-FNO	4.62806	5.592	4.98863	129.106
$FeNbO_4$	4.647	5.613	5.005	130.55

Table S2. Impedance parameters of Ti-FNO at different calcination temperatures.

Ti-FNO	800 ℃	1000 ℃
R_s (Ω)	5.638	5.218
R_{ct} (Ω)	96.51	73.31
CPE	0.8	0.846